

is no other known example of such extreme behaviour. In a corresponding diagram for NGC6553, the RGB is flat near the tip (OBB90).

A new experiment was attempted using the Gunn z band (effective wavelength $\lambda_e = 8900\text{\AA}$), which is close to the red limit reachable with the CCD. In this band considerably less blanketing and reddening are expected. The diagram z vs. $(R-z)$ – Figure 4 – shows little spread at the SGB and RGB, and a flat RGB tip. It is interesting to note the peculiar HB crossing the RGB and showing an extension to the red side.

Distance and Reddening

We estimate the reddening using NGC6553 as reference (OBB90). From

the usual position of the HB in metal-rich clusters (the stubby red clump to the left side of the RGB), we derive $E(V-I) = 2.38$ which corresponds to $E(B-V) = 2.04$, one of the largest so far found for globular clusters. This implies that the cluster is located at $d \approx 5.2$ kpc from the Sun and about 3.6 kpc from the Galactic centre, therefore another genuine bulge (and “disk”) globular cluster. This reddening value is considerably higher than that obtained by Malkan (1982) from integrated properties.

These reddening and distance estimates are however conservative values, because we are taking intrinsic values of HB position from nearby solar-metallicity clusters. For the above discussed reasons, we are probably dealing with a more extreme metallicity

case, and consequently stronger blanketing effects could play an important role.

Conclusion

The interesting CMD properties of Terzan 1 place this cluster as the best candidate for stellar studies, in order to make the link with the nuclear stellar populations in the massive galaxies.

References

- Barbuy, B., Bica, E., Ortolani, S.: 1989, *The Messenger* **58**, 42.
 Malkan, M.: 1982, in *Astrophysical Parameters for Globular Clusters*, eds. A.G.D. Philip, D.S. Hayes (Schenectady: Davis), p. 533.
 Ortolani, S., Barbuy, B., Bica, E.: 1990 *AA* **236**, 362.

Deep $H\alpha$ Survey of Gaseous Emission Regions in the Milky Way and the Magellanic Clouds

PH. AMRAM, J. BOULESTEIX, Y.M. GEORGELIN, Y.P. GEORGELIN, A. LAVAL, E. LE COARER
 and M. MARCELIN, *Observatoire de Marseille, France*
 M. ROSADO, *Mexico Astronomical Institute, Mexico*

1. Introduction

The aim of this survey is to obtain the radial velocities of the ionized gas and the structure of the southern HII regions in our Galaxy and in the Magellanic Clouds.

The spiral structure of our Galaxy can be studied through young stars, individual HII regions and CO molecular clouds; the selection of giant regions similar to those observed in external galaxies allows to draw more precisely the spiral pattern. A first detailed model, with four spiral arms, has been established (Georgelin and Georgelin, 1976) from the distances of exciting stars and from HII regions radial velocities ($H\alpha$ and radio recombination lines). Recent radio-recombination-line surveys by Downes et al. (1980) and Caswell and Haynes (1987) have confirmed and expanded this four-arm pattern. The CO surveys made by Columbia University, Stony Brook and Sydney teams show that the giant molecular clouds follow the same spiral arms. In spite of all these agreements this large-scale distribution of ionized hydrogen remains imprecise and complementary observational data are needed. Moreover, the distances are a fundamental parameter for physical studies of interstellar matter; they di-



Figure 1: The 36-cm telescope of the $H\alpha$ Survey at La Silla. Assembled and tested on the sky at Marseille Observatory in April 1989, it was installed at La Silla in October 1989. Its shelter, built by ESO, has a sliding roof, and an adjacent room has been added to accommodate the data-acquisition and visualization system. Below the main tube one can see two small refractors: one is equipped with a small CCD camera for guiding and the other one with a normal eyepiece for field identification. Prominent at the lower part of the instrument are the bright cryostat containing liquid nitrogen for cooling the photocathode of the Photon-Counting Camera (dry nitrogen circulates inside the pipes to prevent frost formation on the photocathode) and the High-Voltage power supply (black box).

Table 1: Main characteristics of the instrument

| | | |
|-----------------------|---|--|
| Telescope | | |
| – | Ritchey-Chretien type (for a large field) | |
| – | Primary mirror: 36 cm diameter | |
| – | Final aperture ratio F/D = 3.3 | |
| – | Spatial resolution 9"/px | |
| – | Field of view 38' × 38' | |
| Detector | | |
| – | Photon-counting camera composed of a microchannel plate intensifier electrostatically focused coupled to an SIT camera through optic fibres | |
| – | Number of pixels: 256 × 256 | |
| – | Resolution: 1 px = 52 μm | |
| – | Dynamic range: 2 ev/px/h to 3000 ev/px/h | |
| – | Dark noise: 2 ev/px/h | |
| – | Time resolution 1/50 s for each frame | |
| Interference filters | | |
| – | Wavelength | H α , [NII], [SII], H β , [OIII] |
| – | Bandpass | 10 Å FWHM for each filter |
| Interferometers | | |
| – | 2 scanning Fabry-Pérot. At H α wavelength characteristics are: | |
| – | interference order for H α | p = 796 p = 2600 |
| – | free spectral range | 8.2 Å = 376 km/s 2.5 Å = 115 km/s |
| – | spectral resolution | 0.68 Å = 31 km/s 0.25 Å = 11.5 km/s |
| – | typical scanning | 24 steps 24 steps |
| – | sampling step | 0.34 Å = 16 km/s 0.10 Å = 5 km/s |
| – | velocity accuracy | 2 to 3 km/s 1 km/s |
| Typical exposure time | | |
| – | 2h = 60 scanning sequences | |
| – | 1 scanning sequence = 5s per scanning step × 24 steps | |
| Detection limit | | |
| – | 10 ⁻⁹ Jm ⁻² s ⁻¹ sr ⁻¹ with a S/N ratio between 1 and 2 for a 15-min exposure time | |

2. H α Survey Station: A Small Telescope and a High-Performance Software

Thanks to the agreement of the ESO Director General, a 36-cm diameter telescope (see Fig. 1) was installed at La Silla (Chile) in October 1989, near to the GPO. Its Cassegrain focus is equipped with a focal reducer, a scanning Fabry-Pérot interferometer and a Photon-Counting Camera. The concept is similar to our CIGALE instrument (Boulesteix et al., 1984) already used successfully on several large telescopes. The main characteristics are given in Table 1. The telescope and its focal reducer built at Marseille Observatory provide a large field and a high luminosity. The two available scanning interferometers are manufactured by Queensgate Instruments Ltd., London; in such a device, the spacing of the plates may be adjusted step by step through a special electronics controller driving piezo-electric spacers. The Image Photon Counting System – based on a photon-counting camera manufactured by Thomson CSF (France) that we developed with the help of INSU, OHP and LAS in 1975-77 – allows to analyse the photon events frame by frame with a time resolution of 1/50 s. The events are centred with a special detection electronics. The huge amount of data (originally 240 M_o/night when we recorded all the addresses of the detected events) and the systematic nature of this survey led us to conceive a new acquisition system.

A high performance software allows the astronomer to act pertinently on the observational sequence (field identification, S/N ratio estimate, interferometer stability checking, etc.) and to have a complete access to the reduced data while observing, for example to deconvolve and decompose profiles and to measure radial velocities in selected areas of the observed field.

The data-acquisition system is built around VME technology with a Motorola 68020 microprocessor and a real-time operating system PDOS. It is manufactured by Force Computers (Germany). This machine controls the spacing between the plates of the Fabry-Pérot interferometer and receives each 1/50th second the addresses of the photon events found in the frame of the Photon-Counting Camera. These events are used to build up integrated images for each of the 24 values of the spacing of the interferometer (see section 3 to know how a Fabry-Pérot works). While acquiring the data, the free time of the computer may be used to run a set of powerful programmes for reducing the data already recorded in memory.

rectly influence the energetic balance and phenomenological process.

Optical and radio observations are complementary data; however, the overlap is poor, only 30% of the objects having been observed in both ways. The radio observations are limited to the most intrinsically bright objects whereas the optical observations are mainly limited by absorption. Radio data give two possible distances for a given observed radial velocity; the flux, the localization, the morphology and the radial velocities of optical HII regions allow to resolve this distance ambiguity for a lot of objects. Optical observations are an essential link between stellar distances (the only straightforward process) and the radio radial velocities. They can also help discriminating between a “physical link” and a “fortuitous coincidence” when HII regions and molecular clouds are found on the same line of sight and appear close to one another in the sky.

The high sensitivity to monochromatic H α emission, the large field of view, and the high spectral resolution of our new equipment enable us to start detailed emission-line studies. We hope to define the components (bright condensations, classical HII regions, diffuse emission, radio components) and the limits

of the large complexes and we intend to study most particularly the HII regions in areas of stellar formation.

Our Survey should be helpful for the understanding of the physics of the Magellanic Clouds. Since it will provide a homogeneous set of data with wide-field high sensitivity and sufficient angular resolution for both clouds. This will allow to study the global kinematics of these galaxies together with their interstellar medium. A better understanding of several phenomena is expected: mechanisms of galactic fountains, motions and interactions of superbubbles, classical HII regions and SNRs in relation with the amount of energy deposited through several mechanisms (SN explosions, stellar winds, star formation, cloud collisions, etc.) in the various components of the SMC and LMC, detailed study and identification of the nebulae (for instance identification of large diameter SNR). Fabry-Pérot observations are especially well suited for the study of superbubbles or large nebular complexes such as N11 in the LMC. Furthermore, an absolute calibration will be possible all over the LMC since our large field always contains at least one nebula already calibrated by other authors through photoelectric measurements.

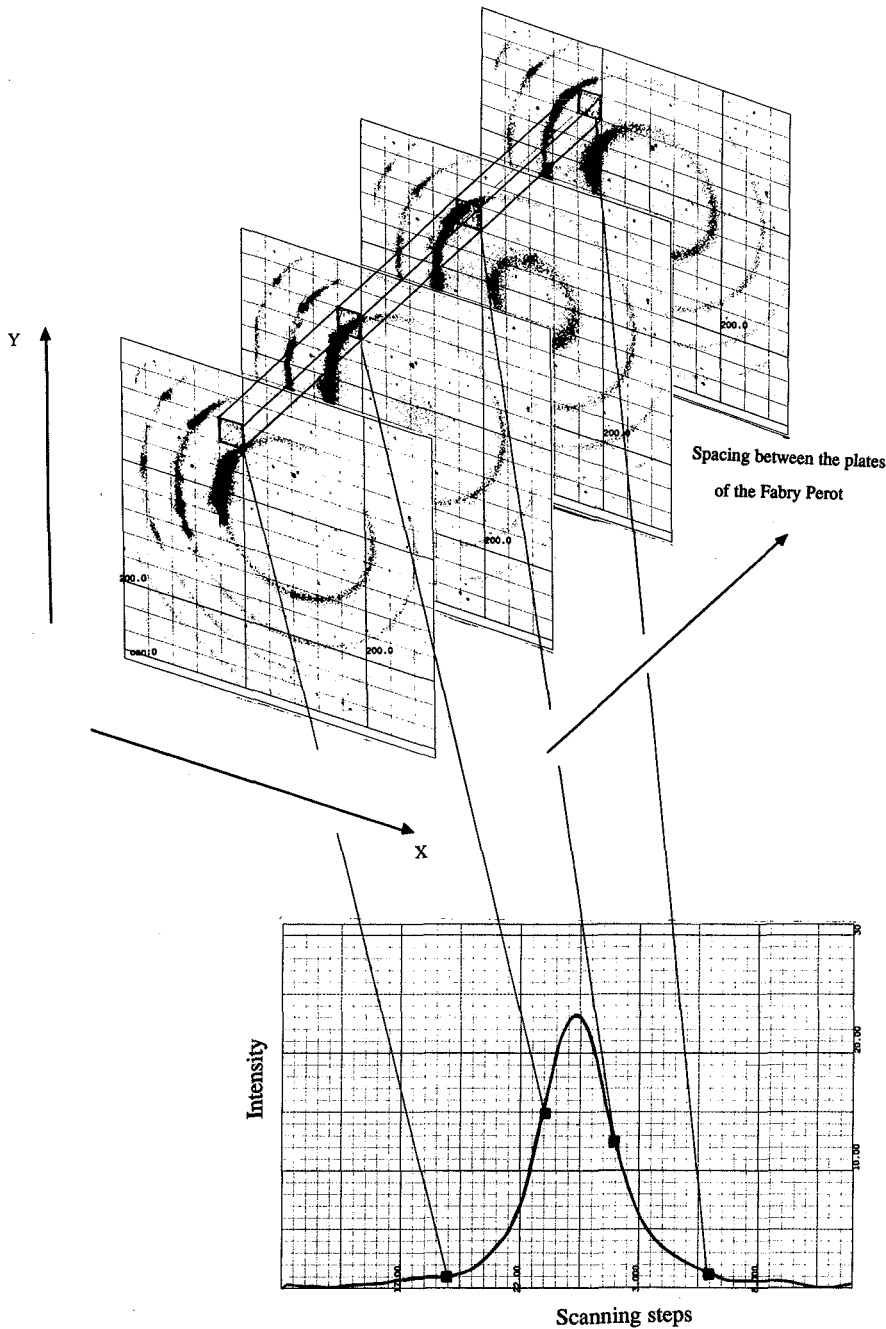


Figure 2: Schematic representation of how a scanning Fabry-Pérot interferometer allows one to obtain detailed profiles of an emission line from all over a nebula. The series of interfering images shown here is a selection from the 24 images given by the interferometer through its scanning process. To show what happens we have exaggerated the pixel size and focused our attention on a given pixel. The profile at the bottom is obtained by plotting the intensity measured inside this pixel for each scanning step. Comparison with calibration rings produced by a well-known emission line allows one to find the precise wavelength origin for the profiles observed inside each pixel of the field.

When an observation is completed, the data are saved on tape with high efficiency using a dedicated compression algorithm permitting to reduce by 5 the size of the files.

The computer also takes on the automatic guiding of the telescope. In this purpose a small cheap CCD has been attached at the focus of a guiding refractor. The frames are digitized and added in memory to increase the S/N ratio (typically 50 frames). The flat-field

correction is done automatically and a dedicated software computes the required corrections to be applied to the telescope driving system. The originality of this automatic guiding system is that it directly stops the interferometer scan and data acquisition whenever the guiding star is lost (because of clouds for instance), everything going on normally as soon as the star is retrieved.

What makes this computer powerful, besides the multitasking system, is the

very fast context switching of the real-time kernel of PDOS permitting to convert all interrupts in terms of events in order to preserve the integrity of the kernel and use all of its facilities to synchronize properly each different task.

3. How Does a Fabry-Pérot Interferometer Work?

The Fabry-Pérot interferometer is composed of two semi-transparent parallel plates coated with dielectric layers. A constructive interference occurs – i.e. an incident monochromatic light will be transmitted – only when the wavelength λ , the angle of incidence i and the spacing e between the plates follow the formula

$$\frac{2 ne \cos i}{\lambda} = p$$

where p is an integer.

p is called the interference order and n is the refractive index of the medium ($n \sim 1$ for the air).

The three main parameters are always linked together through the above formula:

- λ is the wavelength of the nebula we observe. It is the spectral information we are looking for.

- i is the angle of incidence of the light. The cylindrical symmetry of the problem explains why we observe rings through a Fabry-Pérot. The successive rings are found at spatial locations in the field where p is an integer following the above formula. Spectral and spatial information are linked.

- e is the spacing between the plates. It is in fact the only parameter we may adjust easily (this spacing may be changed step by step).

A necessary and sufficient condition to have a complete information all over the field of view is to scan a total quantity Δe defined by:

$$\frac{\Delta e}{e} = \frac{1}{p} = \frac{\Delta \lambda}{\lambda} = \frac{i_{n+1} - i_n}{i_n}$$

(where n refers to the ring number)

One can see that, through the scanning process:

p is changed by one unit

λ has scanned a free spectral range

$$\Delta \lambda = \frac{\lambda}{p}$$

i has scanned the whole field of view. The interference rings have scanned the field and each ring has moved to replace the following one.

An often used parameter is the effective Finesse

$$\mathcal{F} = \frac{\Delta \lambda}{\delta \lambda} = \frac{(\text{free spectral range})}{(\text{spectral resolution})} = \frac{i_n - i_{n-1}}{\Delta i} = \frac{(\text{angular separation between two rings})}{(\text{width of ring profile})}$$

For our interferometers the Finesse is about 12 or 10, that is why we scan through 24 scanning steps.

Figure 2 is another way to understand what really happens in such a device where spatial and spectral information are so intimately linked. When the interferometer is scanning, one can see that the observed flux in a given pixel suddenly increases when an interference ring crosses this pixel.

4. Why a 36-cm Telescope?

Is it madness to initiate an observing programme with a 36-cm telescope at a time when everybody is talking about 8-m telescopes? This would be true if one observed point-like sources, since in that case the light gathered would be proportional to the mirror area. But this is not true for extended sources (such as the H α emission of the Milky Way) because of the so-called optical extension conservation principle ($S\Omega = \text{constant}$). For extended sources, the received light is the same for a 36-cm as for a 3.60-m – the loss in collecting area is exactly compensated for by the increase in the observed angular field Ω . The limiting detection is thus the same for both large and small telescopes and in fact is most often set by our ability to subtract the parasitic nightsky lines (OH 6553.5 Å, geocoronal H α 6562.8 Å, OH 6568.7 Å, OH 6577.2 Å).

Since we study interstellar matter, it is worth making a comparison with radio telescopes. Observing CO clouds is done at two different scales. On the one hand, a survey of the southern Milky Way has been done with 8'8" spatial resolution: Grabelsky et al. (1988), Bronfman et al. (1989). On the other hand, a more detailed analysis of regions where high-mass stars are forming is currently being done at La Silla with the SEST radio telescope at 44" spatial resolution. Our 9" pixel size and our wide field (38' \times 38') will enable us to observe the ionized hydrogen in a manner directly comparable with both types of radio observations.

5. Why a Photon-Counting Camera?

On the basis of purely physical characteristics our photon-counting camera is clearly overtaken by modern CCD cameras (number, size and stability of pixels, d.q.e., dynamical range, etc.). However, it offers a real advantage for this precise type of observation with a scanning interferometer. Since our IPCS has no reading noise at all, we may scan the interferometer as rapidly as we want (typically 5 seconds for each scanning step), reading and recording the

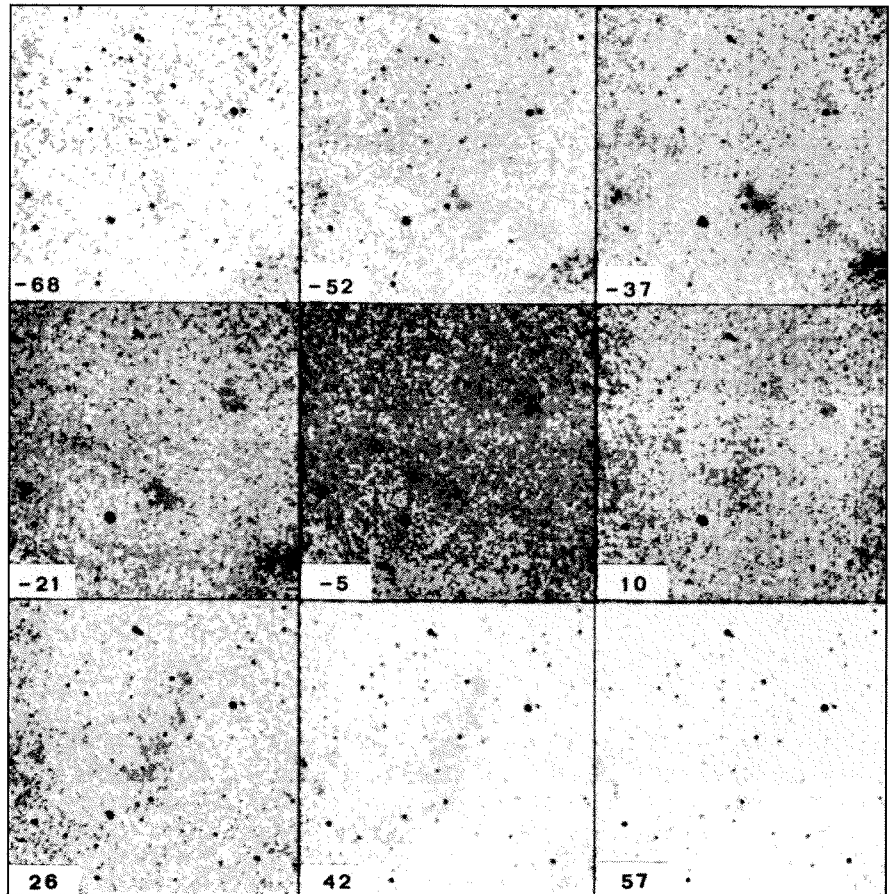


Figure 3: Area of the Milky Way around longitude $l = 302^\circ$ (Field $38' \times 38'$). Series of λ Maps (H α wavelength) of the same field with narrow bandpass (0.34 \AA or 15.6 km s^{-1}) centred at the V_{LSR} radial velocity indicated within each frame. Three emissions are observed in that field. The general diffuse emission produced by the local arm and related with the Coalsack can be seen on the 3 central λ Maps around $V_{\text{LSR}} = -5 \text{ km s}^{-1}$. Two other nebular components, 3 times fainter, are seen around -37 km s^{-1} and around $+26 \text{ km s}^{-1}$. These three faint nebulae are not seen on the Sky Survey (ESO SRC, red). The emission observed at -37 km s^{-1} comes from the Scutum-Crux spiral arm, while the emission around $+26 \text{ km s}^{-1}$ comes from the tip of the Sagittarius-Carina spiral arm and corresponds to an HII region much farther out on the line of sight. This region, already known as the radio source 302.5 -0.7 had never been detected at optical wavelengths. It is some 11.7 kpc distant.

images for each of the 24 steps, then scanning again the whole free spectral range and adding up in memory the successive exposures for each scanning step. For a typical observation, the scanning sequence is repeated 60 times. This enables us to average the transparency conditions encountered along the exposure for each scanning step (which would be due to the mere inevitable change in air mass).

Another advantage for the astronomer is that as soon as the first complete scan is finished, it is possible to visualize on the TV monitor the observed profiles in selected areas.

6. Some Results

Three observing runs have already been made with this instrument (a typical run occupies a new moon) since

April 1990. Most of the observed fields are in the Milky Way and in the Small Magellanic Cloud.

For each typical observation we obtain the following information (all of which are accessible in real time on the TV monitor during the observation):

- 24 calibration interferograms from which we derive one phase-map giving for each pixel the wavelength origin. Instrumental profile and flat-field are also obtained from this series of calibration rings.
- 24 nebular interferograms of the observed field. Owing to the calibration phase-map they allow to compute 24 λ -maps analogous to the radio maps, thus giving one data cube (x, y, λ).
- 65,536 detailed H α profiles (one profile for each of the 256×256 pixels).
- one velocity map derived from the Doppler shift of the profile inside each pixel.

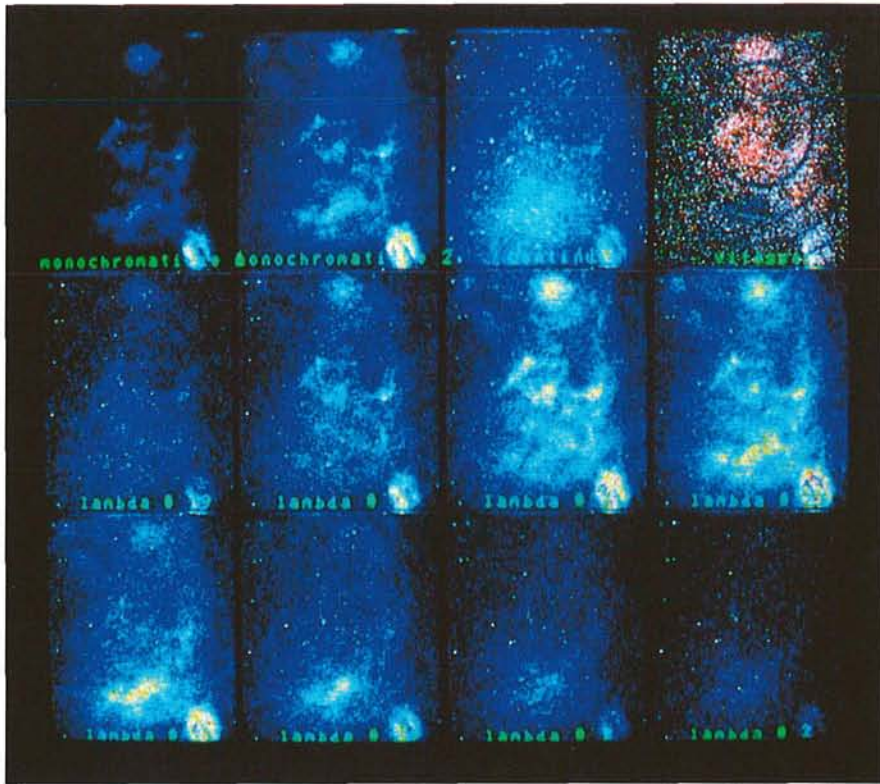
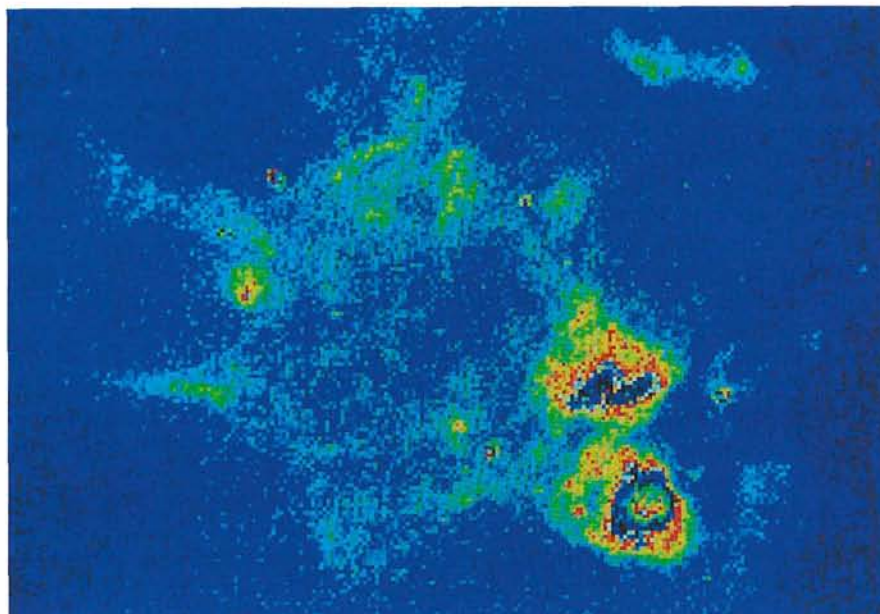


Figure 4: Area of the Milky Way around galactic longitude $l = 328^\circ$. This image has been taken on the TV monitor while observing a $38' \times 38'$ field at galactic longitude $l = 328^\circ$. It shows a typical example of real time visualization of the data already reduced while the instrument is scanning. The images built from the scanning sequence are, from left to right and starting from upper left corner: two monochromatic images of the field obtained with different thresholds, a continuum image of the field, the radial-velocity field with colour coding of the velocities (note that the fine blue rings are artefacts of the data processing, this problem has been fixed since). One clearly sees on this image that there is a group of nebulae around -40 km s^{-1} (pink colour) meanwhile there is a nebula down in the centre at about -20 km s^{-1} (blue colour). This means that now two spiral arms are resolved in this direction: the Sagittarius-Carina arm at -20 km s^{-1} and, just behind, the Scutum-Crux arm at -40 km s^{-1} . The following images on the screen (5th to 12th) are λ Maps (like the λ maps commonly used by radio astronomers) which are also computed from the scanning sequence. The bandwidth for each image is 0.34 \AA (15.6 km s^{-1}). The heliocentric radial velocity is increasing from left to right (and then downwards) and goes through the following values: -83 km s^{-1} , -67 km s^{-1} , -51 km s^{-1} , -36 km s^{-1} , -20 km s^{-1} , -4 km s^{-1} , $+12 \text{ km s}^{-1}$, $+27 \text{ km s}^{-1}$. One clearly sees that the "peculiar" nebula down in the centre does not show up in the same frame as the others but with a shift of about two images.



- one monochromatic image computed by integrating the flux found inside the emission line profile for each pixel.

- one continuum image computed by integrating the flux outside the emission line profile for each pixel.

Several tools for data analysis are available for the astronomer while observing to subtract the nightsky lines and to make a detailed analysis of the profiles.

The instrumental profile is the convolution of an Airy function (for the Fabry-Pérot) with a gaussian function (for the IPCS sampling). This instrumental profile is used to subtract the nightsky lines. Then the nebular profile can be decomposed into several $H\alpha$ component profiles, each one being the convolution of the instrumental profile with a gaussian profile.

By now one can say that it will take a lot of time for the understanding of all the observed data since each run produces some 30 fields, each field containing 65,536 detailed $H\alpha$ profiles inside which there are most often two or three different velocity components (after having subtracted all the nightsky lines) due to the different spiral arms of the Milky Way seen along the same line of sight. Both the intensities and velocities of the different components change all over the field, making the analysis of the data very complex.

Here are a few of the results already obtained in April 1990 and November 1990.

Several radio sources (detected through radio observations of the 6-cm H 109 α hydrogen recombination line) have been detected at $H\alpha$ wavelength for the first time. Figure 3 illustrates such

Figure 6: A superbubble in the SMC. This figure shows a monochromatic image in $H\alpha$ of a superbubble in the SMC. The diameter of this superbubble is about $20'$ (360 pc at a distance of 60 kpc to this galaxy). This superbubble is formed of several smaller bubbles such as N36, N37 and N41 (Henize, 1956) to the west, DEM 80 to the east (Davies et al., 1976) and the SNR N 50 (SNR 0050 – 728) to the north. While this complex appears in DEM photographs, here it is really appreciated as a superbubble, although of less extent than superbubbles in other galaxies. From $H\alpha$ profiles we have found two components of the radial velocity separated in 20 km s^{-1} at the centre of the superbubble. The SNR 0050 – 728 shows violent motions revealed as splitting of the profiles.

a detection, showing the farthest HII region detected during the run of April 1990. It is 11.7 kpc distant, a true performance at optical wavelengths.

Figure 4 illustrates a typical example of a group of nebulae seen together in the sky (toward galactic longitude $l = 328^\circ$), although they belong to different spiral arms of the Milky Way as shown by their different radial velocities.

Figure 5 is an example of analysis of the profiles over a mosaic of two connected fields ($38' \times 38'$ each) around galactic longitude $l = 291^\circ$. The variety of $H\alpha$ profiles obtained illustrates how difficult it is to analyse this type of data. Several components may be distinguished with widely varying intensities all over the field. Continuity considerations generally enable one to unambiguously decompose the profile into its main components, but particular cases may be encountered where the solution is not unique. The recently purchased high-resolution Fabry-Pérot interferometer should help solve these particularly difficult cases, since it offers a much better separation of the different components.

Figure 6 displays a monochromatic image of a superbubble in the SMC where two components of radial velocity profile have been detected at the centre. Violent motions have been found at the periphery due to the SNR 0050-728.

7. Conclusion

The large quantity of data expected from our $H\alpha$ Survey led us to extend the capabilities of our CIGALE instrument, with real time processing of the data. The whole instrumentation of the Survey (focal reducer, interferometer, IPCS and data acquisition and processing electronics) may be attached at the Cassegrain focus of the ESO 3.6-m telescope where it becomes a powerful tool for studying the kinematics of the galaxies. A first successful trial was done in February 1990 with, among others, the observation of the detailed velocity field of the ionized gas in the famous Arp's Antennae (Amram et al., 1991).

Our $H\alpha$ Survey will go on for several years. When completed it will offer a fairly good coverage of the Southern Milky Way and the Magellanic Clouds through a series of $38' \times 38'$ fields with detailed $H\alpha$ profiles inside the 65,536 pixels of each field. More than half of the SMC is already covered (12 fields have been scanned) together with some fields of the LMC. As for the Milky Way we want to have a complete coverage of the most interesting areas, which should comprise more than 200 fields. Then we hope to be able to assess whether the

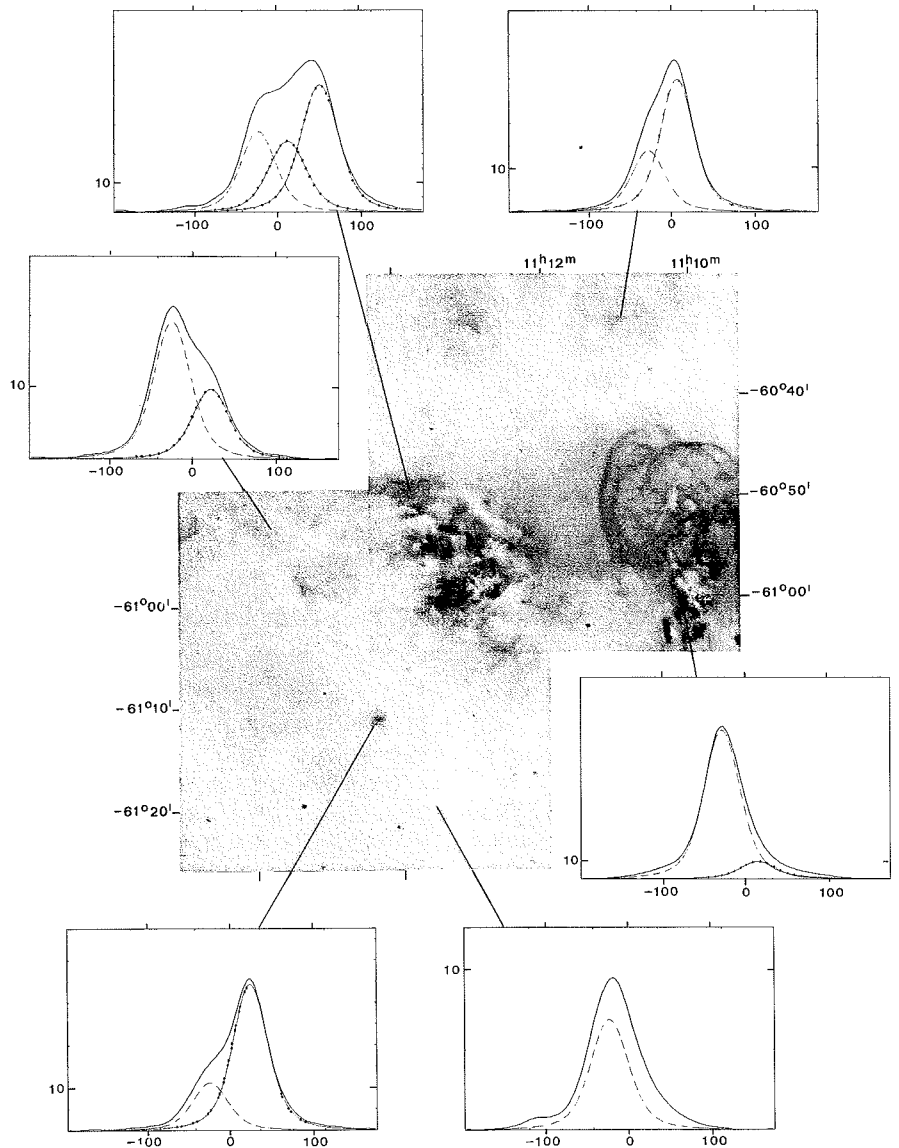


Figure 5: Area of the Milky Way around galactic longitude $l = 291^\circ$. This is an example of two connected fields around $l = 291^\circ$, showing a great variety of HII regions at very different distances in the Carina spiral arm seen edge on. The two giant HII regions seen on the $H\alpha$ monochromatic images built from the scanning sequence are westward NGC 3576 ($V_{LSR} = -25 \text{ km s}^{-1}$, stellar distance = 3 kpc), saturated in its brighter part down to the right, and eastward NGC 3603 (average $V_{LSR} = 15 \text{ km s}^{-1}$, stellar distance = 7 kpc). NGC 3603 is one of the most massive HII regions in our Galaxy already known for its strong internal motions (Balick et al., 1980), their comparison with the very complex CO profiles observed with the SEST (Melnick, 1989) will be very fruitful. A beautiful colour image of these HII regions has been published in the central pages of the Messenger No. 60 (Block and Madsen). Our $H\alpha$ profiles in selected areas are shown all around and illustrate different cases encountered, showing how difficult the interpretation of the results may be. A general emission component, related with NGC 3576, can be seen all over the two fields (dashed line component inside each frame). Other $H\alpha$ components (dotted lines) of variable velocity and intensity are superimposed. They may be separated into simple components analysing the profiles step by step all over the field with the help of morphology, intensity variations, radio results and so on.

Milky Way actually has 4 spiral arms or not.

Acknowledgements

We are much indebted to Prof. L. Woltjer who authorized and helped the installation of our instrument at La Silla when he was Director General of ESO. We also thank the present Director General, Prof. H. van der Laan, for continu-

ing this help through the extension of the building and providing the astronomers accommodation at La Silla. We thank INSU for financial support of a large part of our instrumentation and for covering the travels fees. The installation of the telescope has been done efficiently with the help of the ESO mechanics workshop and the electronics workshop. The telescope has been designed at Marseille Observatory

with the help of P. Joulie and manufactured with the help of our observatory mechanics workshops, more especially J. Urios who also helped us at La Silla. We also want to thank A. Viale for her constant help when reducing the data in Marseille.

References

Amram, P., Boulesteix, J., Marcelin, M., 1991, Dynamics of Galaxies and their Molecular cloud distributions, F. Combes

and F. Casoli Ed., IAU Symposium 146, p. 182.
Balick, B., Boeshaar, G.O., Gull, T.R. 1980, *Astrophys. J.*, **242**, 584.
Boulesteix, J., Georgelin, Y.P., Marcelin, M., Monnet, G., 1984, Instrumentation in Astronomy, V.A. Boksenberg, D.L. Crawford Ed., Proc. SPIE 445, p. 37.
Bronfman, L., Alvarez, H., Cohen, R.S., Thaddeus, P. 1989, *Astrophys. J. Suppl. Ser.* **71**, 481.
Caswell, J.L., Haynes, R.F. 1987, *Astron. Astrophys.*, **171**, 261.

Davies, R.D., Elliott, K.H., Meaburn, J. 1976, *M.N.R.A.S.* **81**, 89.
Downes, D., Wilson, T.L., Bieging, J., Wink, J. 1980, *Astron. Astrophys. Suppl.*, **40**, 379.
Grabelsky, D.A., Cohen, R.S., Bronfman, L., Thaddeus, P. 1988, *Astrophys. J.*, **331**, 181.
Georgelin, Y.M., Georgelin, Y.P. 1976, *Astron. Astrophys.*, **49**, 57.
Henize, K.G. 1956, *Astrophys. J. Suppl.*, **2**, 315.
Melnick, J. 1989, *The Messenger*, **57**, 4.

Salpeter Mass Functions of Young Populous Clusters in the LMC?

T. RICHTLER, K.S. DE BOER, *Sternwarte der Universität Bonn, Germany*

R. SAGAR, *Indian Institute of Astrophysics, Bangalore, India*

1. The Magellanic Clouds as Laboratories for Deriving IMFs

Although astronomers are not able to perform experiments with their objects under study, the Magellanic Clouds provide quite well what we may call an "astrophysical laboratory" (see Westerland, 1990, for a review on Magellanic Cloud research). An important topic which can be tackled by investigating Magellanic Cloud objects is the shape of

the Initial Mass Function (IMF) of newly formed stars.

The question whether the mass spectrum of stars that are born in a star-forming region has a universal shape or varies according to some (still unknown) laws, is fundamental for understanding both star formation and galactic evolution. A theory of star formation which is unable to predict the IMF of stars will always be considered as incomplete. The stellar mass spectrum is of rele-

vance for galaxy evolution, since it controls the supernova rate and generally the amount of energy injected into the interstellar medium by massive stars. Moreover, the yield of freshly synthesized elements is a direct function of the stellar mass spectrum.

It has long been acknowledged that the young populous star clusters in the Magellanic Clouds are principally ideal targets for the investigation of the mass spectrum of their stars: They offer a high number of stars and a large mass interval with an upper limit of 10–15 solar masses. Such conditions are not found in the Milky Way. On the other hand, the extreme crowding of the stars complicates severely the derivation of a reliable luminosity function.

The crowding difficulty appears indeed prominently in papers related to this subject. Elson et al. (1989) counted stars on photographic plates in the surroundings of several young populous clusters in the Magellanic Clouds and determined mass functions which were surprisingly flat. If we assume a power law description of the shape $dN = m^{-(1+x)} dm$ (where dN is the number of stars in the mass interval between $m-dm$ and $m+dm$), then Elson et al. found values for x in the range $-0.8 < x < 0.8$. Remember that the population in the solar environment can be described by $x = 1.3$. A systematic difference between stellar mass functions in the Magellanic Clouds and in the Milky Way would be a very important result.

However, in a paper by Mateo (1989) on the same topic, a quite different conclusion was reached. Mateo performed CCD photometry in Magellanic Cloud clusters of a wide range in age, among

The 2nd ESO/CTIO Workshop on

Mass Loss on the AGB and Beyond

will be held in La Serena, Chile, on 21-24 January 1992.

The aim of this workshop is to bring together observers and theoreticians to discuss the evolutionary stage of low and intermediate mass stars between the AGB and planetary nebulae: the **transition objects**.

Specific topics will include: transition objects, protoplanetary nebulae, mass-loss mechanisms and estimators, PN formation, new techniques: FIR, mm and sub-mm.

Invited speakers are: J. Dyson, Manchester; H. Habing, Leiden; P. Huggins, New York; M. Jura, Los Angeles; M. Morris, Los Angeles; H. Olofsson, Onsala; A. Omont, Grenoble; F. Pijpers, Leiden; D. Rouan, Meudon; R. Waters, Groningen; B. Zuckerman, Los Angeles.

Organizing Committee: D. Geisler, B. Reipurth, R. Schommer, H.E. Schwarz, (chair).

Contact addresses: H.E. Schwarz, ESO, Casilla 19001, Santiago 19, Chile.

Tel.: +56 2 699 3425 or 698 8757;

Tlx.: 240881 esogo cl.

Fax: +56 2 699 3425 (office hours);

E-mail: schwarz@dgaeso51.bitnet.

R. Schommer, CTIO, Casilla 603, La Serena, Chile.

Tel.: +56 51 225415; Tlx.: 620301 auract cl;

Fax: +56 51 225415 ext.; E-mail: rschommer@

nao.edu